Research Square

Preprints are preliminary reports that have not undergone peer review.
They should not be considered conclusive, used to inform clinical practice,
or referenced by the media as validated information.

Molecular architecture determines proteostasis responses

Tiago Outeiro

tiago.outeiro@med.uni-goettingen.de

University Medical Center Göttingen https://orcid.org/0000-0003-1679-1727

Madiha Merghani

University Medical Center Göttingen

Manuel Flores Leon

University Medical Center Göttingen https://orcid.org/0000-0002-1094-8773

Tamer Abdelaal

University Medical Center Göttingen

Victoria Simoes

Federal University of Rio de Janeiro

Ilona Eggert

UMG

Elis Eleutherio

Universidade Federal do Rio de Janeiro https://orcid.org/0000-0001-5842-2714

Silke Kaulfuß

University Medical Center

Article

Keywords: synucleinopathy, organelle, in vitro, pathology

Posted Date: November 23rd, 2026

DOI: https://doi.org/10.21203/rs.3.rs-10744878/v1

License: This work is licensed under a Creative Commons Attribution 4.0 International License.
Read Full License

Additional Declarations: There is no conflict of interest

Molecular architecture determines proteostasis responses

Merghani M[1*], Flores-León M[1*], Abdelaal T[1], Bernardo VS[1,2], Eggert I[3], Eleutherio ECA[2], Kaulfuß S[3], and Outeiro TF[1,4,5,6#]

1. University Medical Center Göttingen, Department of Experimental Neurodegeneration, Center of Biostructural Imaging of Neurodegeneration, Göttingen, Germany.

2. Institute of Chemistry, Federal University of Rio de Janeiro (UFRJ), Rio de Janeiro, RJ, Brazil.

3. Institute of Human Genetics, University Medical Center Göttingen, 37073 Göttingen, Germany.

4. Translational and Clinical Research Institute, Faculty of Medical Sciences, Newcastle University, Newcastle Upon Tyne, United Kingdom.

5. Deutsches Zentrum für Neurodegenerative Erkrankungen, Göttingen, Germany.

6. Faculdade de Medicina e Ciências Biomédicas, Algarve Biomedical Center Research Institute, Universidade do Algarve, Faro, Portugal.

***Equal contribution**

#Correspondence:

Tiago F. Outeiro

Email: touteir@gwdg.de

Keywords: synucleinopathy, organelle, in vitro, pathology

Abstract

Numerous human cell lines are widely used as laboratory models because they are easy to maintain, can be generated rapidly, and circumvent many of the ethical concerns associated with studies using mammalian animal models. However, these cells are often immortalized, as they are derived from human tumors and, therefore, harbor abnormal chromosome numbers, resulting in aneuploidy, altered gene expression, distinct cellular architecture, and imbalances in proteostasis pathways. For this reason, the interpretation and reproducibility of experimental findings is not always straightforward. In this study, we performed a systematic comparison between three commonly used cell lines (HEK293, H4, and SH-SY5Y) in order to obtain insight into how the molecular architecture influences protein handling. First, we determined the karyotypic composition and then performed a comprehensive analysis of cellular organization and organelle morphology. We further characterized protein quality control systems and assessed how the molecular architecture of the cells affected the subcellular distribution of selected proteins associated with neurodegenerative diseases. Our results demonstrate that differences in chromosomal content, creating different cellular milieus, affect multiple organelles and intracellular pathways. Our findings highlight the impact of genetic background on cellular organization and function and provide a valuable resource offering practical guidance for selecting the most appropriate cell line model for specific research questions.

Introduction

In a time when the ethical justification for research using animal models is being questioned, studies using cell-based models gain renewed attention. In this context, human cell lines are indispensable tools in biomedical research, offering reproducibility, scalability, and accessibility to mechanistic studies. These simple models have enabled fundamental discoveries across cell biology, biochemistry, and translational research. However, their face validity as models depends on how well their intrinsic biological properties and limitations are understood and accounted for. Commonly used cell lines are transformed, and derived from human tumours and, therefore, they tend to be aneuploid. However, this is often an underappreciated feature that creates different molecular architectures, and different cell biology. In addition, continuous passaging, adaptation to *in vitro* conditions, and selective pressures imposed by culture environments, frequently lead to karyotypic instability and the emergence of heterogeneous aneuploid populations[1]. As a result, many experimental systems used for studying fundamental aspects of cell biology, including proteostasis, operate under conditions of altered chromosome dosage. This raises important questions regarding the interpretation and reproducibility of experimental findings, as well as the extent to which aneuploidy itself shapes cellular responses to stress.

At the cellular level, aneuploidy imposes a chronic burden on proteostasis networks. Imbalances in gene dosage disrupt the stoichiometric assembly of protein complexes, leading to the accumulation of orphan subunits, increased protein misfolding, and heightened demand on protein quality control systems, including the ubiquitin–proteasome system and autophagy-lysosome pathways[11,12]. This proteotoxic stress has

been well documented in model systems, where aneuploid cells exhibit altered translational control, increased chaperone dependency, and sensitivity to perturbations in protein degradation pathways. Importantly, these features overlap with hallmarks of neurodegenerative diseases, raising the possibility that shared mechanisms underlie proteostasis dysfunction across diverse biological contexts.

Furthermore, aneuploid cell models used in research are derived from diverse origins and display distinct transcriptional profiles, leading to differences in protein homeostasis. As a result, these cells may respond differently to various stimuli and therapeutic agents[13–15]. Understanding these variations is crucial for the development of effective treatments and for the reliable evaluation of both target-specific and off-target effects.

Therefore, a broad characterization of commonly used cell lines is essential for a better interpretation of the experimental outcomes. In this study, we present a comprehensive baseline characterization of three widely used aneuploid cell lines, HEK293, H4 and SH-SY5Y. By systematically characterizing the relationship between chromosome imbalance and cell biology, including protein homeostasis pathways, with a special focus on pathways implicated in neurodegenerative diseases, we aimed to highlight how karyotypic variation contributes to experimental variability and to uncover general principles linking aneuploidy to proteostasis dysfunction.

Results

Karyotypic composition and biologically relevant gene dosage of HEK293, H4, and SH-SY5Y cells.

First, we assessed the karyotypic profiles of HEK293, H4, and SH-SY5Y cells to establish their baseline genomic context and identify chromosomal features that could have an influence on the expression of biologically relevant proteins. We found that HEK293 cells have a hypotriploid karyotype, with a modal chromosome number of 64 (Fig 1A). Among the most prominent chromosomal anomalies are more than four copies of chromosome 9, 21, 22, and X. H4 cells are almost triploid with a modal chromosome number of 73 (Fig 1B). This cell line has four copies of chromosome 7 and 14, only one copy of chromosome 3 and 8. The rest of the chromosomes have either two or three copies. SH-SY5Y cells, which are often considered a better model than HEK293 or H4 cells given the possibility of differentiation into a tyrosine hydroxylase-positive phenotype, have a modal chromosome number of 47 (Fig 1C). Among the chromosomal features of the cell line that are noticeable are rearrangements of segments in chromosome 1, 9, and 22, and a triplication of chromosome 7.

Strikingly, some neurodegenerative disease-associated proteins are encoded by genes in those chromosomes (Table 1). The *SNCA* gene is encoded in chromosome 4, *TARDBP* in chromosome 1, *LRRK2* in chromosome 12, and *SOD1* in chromosome 21. When comparing the specific chromosome numbers in each cell line, H4 cells are the only cell line that has a triplication in chromosome 4. Chromosomes 1 and 21 are commonly triplicated in HEK293 and H4 cells. This suggests that these three cellular models have specific chromosomal features that can affect their basic biological characteristics and,

thereby, how pathologically associated proteins may behave and are handled by the respective proteostasis network.

Cytoskeletal heterogeneity across cellular models

Cells execute a wide range of specialized functions through dynamic processes, either by redistributing proteins to specific subcellular compartments or by remodeling organelles in response to changing cellular demands, both of which are directly influenced by the genetic background and proteostatic capacity of the cell. Even the function of some cells has a correlation with their shape[16]. Therefore, cytoskeletal proteins play a central role in defining the basal state of a cell[17]. In our comparison, the three cell lines show a similar spatial organization of the cytoskeletal proteins (Fig 2A), though differences between them are observed in the relative abundance of these proteins. Quantification of cytoskeletal proteins showed that HEK293 cells, one of the smallest cells compared to H4 cells (Fig 2B), have the lowest expression level of alpha tubulin and beta-actin (b-actin) (Fig 2D, E), suggesting that the difference in protein content could be in part explained by the variation in their size for this cell line. Interestingly, HEK293 cells show the highest level of acetylated alpha-tubulin (Fig 2C - E), indicating that these cells maintain a more stable microtubule network compared to H4 and SH-SY5Y cells. In SH-SY5Y cells, the levels of b-actin were the highest compared to other cells (Fig 2D, E), possibly reflecting their highly undifferentiated state.

Differential engagement of the UPS and autophagy-lysosome pathway

Misfolded and aggregated proteins are not only degraded by the autophagy lysosomal pathway (ALP) but also by the ubiquitin proteasome system (UPS)[18,19]. In our study, we evaluated the global difference of these degradative pathways among the cell lines. First, we stained the different cell lines with LC3, the marker for autophagosomes, LAMP1, a marker for lysosomes, and Lysotracker, a fluorescent dye that accumulated in acidic organelles such as lysosomes and late endosomes. In SH-SY5Y cells, LC3 and LAMP1 were frequently colocalized in regions where Lysotracker fluorescence intensity was reduced (Fig 3A, B), indicating decreased lysosomal acidity. Quantification of the LC3II/I ratio revealed a relatively higher LC3II content in SH-SY5Y cells compared to the other two cell lines (Fig 3C, D). Although we did not find a statistically significant difference in LAMP1 level across the different cell lines (Fig 3E, F), a trend towards higher LAMP1 content was observed in SH-SY5Y cells. Furthermore, when characterizing the protein ubiquitination pattern, HEK293 cells have the strongest smear for the ubiquitinated substrates and H4 cells have the weakest signal compared to the other cell lines (Fig 3G). Overall, these results suggest that SH-SY5Y cells have an autophagy-dominant proteostasis strategy, while HEK293 cells appear to rely more heavily on the UPS and have a more active constitutive secretory/proteasomal axis.

Differential starvation response kinetics across HEK293, H4, and SH-SY5Y cel

Given the differences identified in UPS activity and autophagy-lysosomal pathway across the three cell lines, we next assessed their response to nutrient deprivation. We assessed the effect of starvation by quantifying the phosphorylation of the mTOR effector, S6, as a readout, and the content of p62, the autophagosome marker. We found that in HEK293

cells, the phosphorylation of S6 (P-S6) was abolished within the first three hours. However, the level of p62 was almost constant up to 6 hours and started to reduce at 24 hours of starvation (Fig 4A, B). This indicates a delayed effect of inhibiting mTOR on the starvation process. In H4, P-S6 and p62 levels diminished after 3 hours of starvation but remained constant up to 6 hours after starvation and were reduced within 24 hours of starvation (Fig 4C, D). This indicates that starvation also has a delayed effect on mTOR activity. However, the effect of mTOR inhibition on the autophagy response was accelerated in H4 cells. Interestingly, under normal nutritional conditions, SH-SY5Y cells had a low level of P-S6, and the phosphorylation was completely abolished within the first three hours of starvation. The level of p62 was also low in control condition and was undetectable after three hours of starvation (Fig 4E, F). This suggests that SH-SY5Y cells have a high level of basal autophagic level and aligns with the previous result, where the SH-SY5Y cells showed lower lysosomal acidity and higher LC3II/I ratio.

Mitochondrial network architecture differs across cell lines

Mitochondria are cellular organelles not only responsible for energy production, but they also play important roles in apoptosis, calcium homeostasis, innate immunity, and phospholipid synthesis. We compared the mitochondrial network to unravel if the basal stress status and mitochondrial morphology might differ among the three cell lines. Initial qualitative image analysis suggested that H4 cells had the highest difference in mitochondrial network (Fig 5A). Protein quantification of TOM20 confirmed that indeed the three cell lines have a different content, where HEK293 have the highest levels, followed by SH-SY5Y and then H4 cells (Fig 5B, C). Furthermore, quantification of the

mitochondrial mean size showed that H4 cells have clearly smaller mitochondria, with shorter and less branches (Fig 5D - I). HEK293 and SH-SY5Y cells have elongated, large mitochondria with a more branched and longer network (Fig 5D - I). Altogether, these results suggest that H4 cells have a particular mitochondrial network architecture.

ER and Golgi morphological characteristics in the cell lines correlate with their size and secretory profiles.

Given that cell types differ in protein synthesis load, secretory pathway activity, cytoskeletal architecture, mitochondrial morphology, and protein quality control systems, the morphology of the endoplasmic reticulum (ER) and Golgi apparatus was systematically evaluated and compared in each cell line as a functional readout of these differences. The initial qualitative evaluation suggested that both organelles seemed to have a morphology in accordance with the size of the cell line (supplementary Fig 1). To further describe the morphology of ER based on the marker Calnexin, concentric zones from the nucleus to the cell periphery were created: perinuclear ER (zone 1), inner cytoplasmic ER (zone 2), outer cytoplasmic ER (zone 3) and peripheral ER (zone 4) (Fig 6A). The ER progression, measured by Calnexin fluorescence intensity, follows a decreasing trend with the highest fluorescence in zone 1 and the lowest fluorescence in zone 4 (Fig 6B). H4 cells have a higher fluorescence intensity in zone 1 due to a higher area in zone 2 compared to HEK293 and SH-SY5Y cells. Nevertheless, the three cell lines follow this decreasing trend in the fluorescence intensity. Then, the mean zone areas were measured, and it revealed an increasing mean area with zone 4 being the biggest for the 3 cell lines (Fig 6C). Again, the H4 cell line has the biggest mean area in each

zone, followed by the SH-SY5Y cells and then the HEK293 cells. Together the data suggests that the total area of each cell line is correlates with the distribution of the area occupied by each ER zone.

The area, compactness, and the ribbon length of the Golgi apparatus were quantified using GM130 as a marker (Fig 7A). The initial image qualitative evaluation revealed that the Golgi apparatus of the HEK293 cells appears to be smaller and almost with a spherical shape compared to the H4 and the SH-SY5Y cell lines. The quantification of the area showed that SH-SY5Y cells have the biggest Golgi apparatus, followed by the H4 cells and then by the HEK293 cells (Fig 7B). Additionally, as seen in the representative images, the compactness ratio showed that the Golgi apparatus of HEK293 tends to have an almost spherical shape compared to the enlarged morphology of the one of H4 and SH-SY5Y cells (Fig 7C). Finally, when the ribbon length was measured, SH-SY5Y cells had the biggest length, followed by H4 cells, and HEK293 being the smallest (Fig 7D). Altogether, these morphological measurements show that the Golgi apparatus characteristics of HEK293 cells correlate with their size compared to the other two cell lines. Interestingly, H4 cells generally have bigger size than SH-SY5Y cells, and the Golgi apparatus is bigger in SH-SY5Y cells, possibly reflecting the secretory activity of the cells.

Stress granule markers are identical across cell lines

Stress granules are dynamic cytoplasmic aggregates composed of untranslated mRNAs, RNA-binding proteins, and translation factors that form in response to cellular stress. They are membrane-less organelles that can act as potential seeds for protein aggregation in neurodegenerative diseases [20]. To further characterize the basal stress

machinery in the cell lines, G3BP1 and TIA1 were quantified. The comparison of these RNA-binding proteins did not show a significant difference between them (supplementary Fig 2A, B).

LRRK2 distribution is different across the cell lines

Mutations in the *LRRK2* gene are among the most common genetic causes of PD [21]. LRRK2 is a large multidomain protein that can bind to microtubules and change the microtubule-associated transport. In our work, we expressed LRRK2 in the three different cell types. We found in H4 cells, LRRK2 tends to form more filamentous structures, and this filament seemed colocalizing with alpha-tubulin (Fig 8A - C). The pattern of expression was different in HEK293 and SH-SY5Y cells, where LRRK2 has a more dispersed and uniform cytoplasmic distribution (Fig 8A - C).

TDP-43 subcellular localization differs across cell types

TDP-43 is a nuclear protein that plays an important role in RNA regulation, including transcription, alternative splicing regulation, and mRNA stabilization. However, under pathological conditions, TDP-43 undergoes different post-translational modifications, such as phosphorylation and ubiquitination, which lead to the translocation of TDP-43 to cytoplasm and the accumulation of aggregated forms [22]. Confocal imaging of TDP43-tdTomato revealed marked differences in subcellular localization (Fig.9A - B). Quantitative mask-based analysis demonstrated that HEK293 cells exhibited the highest proportion of cells with detectable TDP-43 signal outside the nucleus (~55%), whereas H4 cells showed a significantly lower fraction (~8%), and SH-SY5Y cells displayed

intermediate levels (~12%) (Fig. 9C), suggesting that basal cellular distribution of TDP-43 is strongly cell-type-dependent. However, no aggregation was detected, and the signal remained restricted to the perinuclear region rather than being distributed throughout the cytoplasm.

Cell-type-specific aggregation propensity of SOD1A4V

To determine whether the aggregation-prone mutant SOD1A4V exhibits cell-type-dependent distribution patterns, we transiently expressed human SOD1 WT or SOD1A4V in HEK293, H4, and SH-SY5Y cells and performed confocal immunocytochemistry. SOD1 WT displayed a predominantly diffuse cytoplasmic distribution across all three cell lines, with no evidence of inclusion formation (Fig. 9D). In contrast, SOD1A4V showed a divergent pattern depending on the cellular context (Fig. 9E). In H4 cells, SOD1A4V formed discrete cytoplasmic inclusions in 48.65 ± 6.45% of transfected cells (Fig. 9F). These findings demonstrate that H4 cells exhibit a permissive intracellular environment for SOD1A4V aggregation, whereas HEK293 and SH-SY5Y cells appear comparatively resistant.

Subcellular localization of tagged and untagged aSyn varies across cell lines.

Another widely studied protein due to their importance in neurodegeneration is aSyn. Different approaches are used to visualize and evaluate their localization: tagged and untagged protein. Here, the EGFP-tagged and an untagged aSyn were transfected to the three cell lines to evaluate the distribution in the cytoplasm and the nucleus. The initial qualitative evaluation of the three cell lines showed that aSyn-EGFP was present in the

cytoplasm and in the nucleus. Nevertheless, H4 cells appear to have a higher presence in the nucleus (Fig 10A). The cytoplasmic and nuclear quantification revealed that HEK293 cells had a higher localization of aSyn-EGFP in the cytoplasm, followed by SH-SY5Y cells and then by H4 cells (Fig 10B). The qualitative image analysis of untagged aSyn suggested that H4 and SH-SY5Y cells had a higher localization of aSyn in the nucleus compared to HEK293 (Fig 10C). The quantification showed that among the three cell lines, HEK293 and H4 cells had a higher cytoplasmic localization of untagged aSyn compared to SH-SY5Y cells (Fig 10D). These results highlight the importance of evaluating different strategies and the model intended to be used when characterizing biological phenomena.

Discussion

Chromosome imbalances can influence protein homeostasis pathways in cellular models, contributing to experimental variability. Therefore, a global characterization of cell line models is therefore essential for understanding their biological context and translatability. Cells respond dynamically to a wide range of intracellular and extracellular stimuli, where the cytoskeleton and the cell membrane play fundamental roles for adaptation[16]. Reduced expression levels of these structural proteins disrupt cellular dynamics, whereas overexpression can impair organ function, enhance protein aggregation, and promote cellular stress responses [23–26]. The observed differences in cytoskeletal protein levels across HEK293, H4, and SH-SY5Y cells likely reflect adaptations to both the aneuploid nature and the distinct identity of each cell line. Notably, although HEK293 cells display

the lowest alpha-tubulin levels, they exhibit the highest acetylated tubulin content, suggesting a compensatory mechanism to maintain microtubule stability. In contrast, SH-SY5Y and H4 cells appear to maintain a more dynamic microtubule pool suited to neuronal plasticity and morphological remodeling[27–29].

Cell homeostasis requires tight regulation of protein clearance. Autophagy is a conserved intracellular degradation pathway through which cellular components, including damaged organelles, misfolded or aggregated proteins, and other potentially toxic material, can be recycled. The degradation process occurs inside the lysosome, where degradation enzymes require a low pH for optimal function. The UPS is the principal intracellular pathway for the selective degradation of misfolded, damaged, and short-lived proteins, playing a central role in maintaining proteostasis[30,31]. Differences in polyubiquitinated protein abundance across the three cell lines are consistent with cell line-specific proteostatic demands and differential engagement of protein quality control pathways, likely reflecting distinct protein synthesis loads and basal misfolding rates. In SH-SY5Y cells, LAMP1/LC3 colocalization indicates active autolysosome formation, demonstrating productive autophagic flux. Combined with reduced lysosomal acidity and a higher LC3-II/LC3-I ratio, these findings suggest that SH-SY5Y cells preferentially engage the autophagy-lysosome pathway over the UPS for protein clearance.

The autophagy process is directly related to the nutritional condition of cells, and it is tightly regulated through the master of nutritarians sensor, Mammalian target of rapamycin complex 1 (mTORC1). During nutritional decrease, the mTOR signal is inhibited, leading to decreased phosphorylation of the effector proteins and activation of the autophagy[32,33]. Comparative analysis of autophagic markers and starvation

responses further demonstrates that the three cell lines mount distinct autophagic responses to the same stimulus, reflecting their divergent genetic backgrounds.

Mitochondrial dysfunction is a hallmark of many neurodegenerative diseases. Despite differences in their clinical presentation, these disorders commonly exhibit impaired energy metabolism, increased oxidative stress, and dysregulated mitochondrial dynamics[34–37]. In healthy cells, mitochondrial shape ranges from rod-like structures to highly interconnected reticular networks[38]. Accumulating evidence suggests a relationship between cytoskeletal proteins and mitochondrial dynamics [39–41]. Mitochondrial dynamics are primarily regulated by fusion, fission, and degradation. These mechanisms control mitochondrial shape and organization, which are important for functions such as intracellular transport and oxidative phosphorylation. H4 cells exhibited the lowest expression levels of the outer mitochondrial membrane protein TOM20, as well as the smallest mitochondria with reduced branching complexity and the most fragmented network. This is consistent with their reduced acetylated tubulin levels, which may decrease microtubule stability and increase susceptibility to mechanical stress[27,28]. Furthermore, actin filaments facilitate Drp1-mediated mitochondrial fission and mitophagy [42], and H4 cells, which also display the most extensive ER network, may actively exploit ER-actin-Drp1-mediated constriction to drive mitochondrial fragmentation.

The ER is a cellular compartment that not only plays an important role in protein synthesis, but it is also involved in lipid synthesis, protein quality control, and regulation of organelle homeostasis[43,44]. Interestingly, actin filaments and the ER can regulate mitochondrial morphology through fission. Consistent with this mechanism, H4 cells showed the biggest ER network and the highest degree of mitochondrial fragmentation. Thus, suggesting this

is an active mechanism in H4 cells. These results may reflect the metabolic identity and mitochondrial dynamics of H4 cells; features that are important to be considered when using the cell line as an experimental model.

HEK293 cells, despite being a high-capacity protein synthesis platform [45,46], displayed a relatively small ER and compact Golgi apparatus, consistent with operation near secretory pathway saturation [47] and elevated basal ubiquitination load. The compact Golgi morphology is further consistent with their low β-actin content, given the well-established role of actin in Golgi structural maintenance. In contrast, SH-SY5Y cells displayed an extended Golgi apparatus and abundant actin filaments, consistent with their neurotransmitter-oriented secretory phenotype [48,49], which relies on regulated vesicular secretion rather than bulk protein output. H4 cells exhibited the largest ER network, which facilitates the study of ER-associated mechanisms such as the unfolded protein response (UPR) and ER-associated degradation (ERAD)[50,51], and showed an intermediate ubiquitin signal consistent with active protein quality control.

Since protein quality control systems and disease-relevant organelles exhibit cell line-specific morphological differences, characterizing the basal expression and localization of neurodegeneration-associated proteins is essential for correctly interpreting experimental outcomes. The expression and distribution of LRRK2, TDP-43, SOD1, and aSyn were all cell line-dependent. LRRK2 formed filamentous structures colocalizing with microtubule components specifically in H4 cells, which also showed relatively higher alpha-tubulin and lower acetylated tubulin levels, suggesting that cytoskeletal composition influences LRRK2 distribution[52–54].

H4 cells also displayed aggregated SOD1 A4V. These inclusions were typically cytoplasmatic and morphologically consistent with misfolded protein aggregates. The absence of inclusion-like structures in HEK293 or SH-SY5Y cells, despite the expression of SOD1A4V, indicates that aggregation of SOD1A4V is not merely a consequence of overexpression but reflects intrinsic, cell-type-specific susceptibility to proteostatic imbalance. Additionally, excessive production of superoxide radicals is a marker for mitochondrial dysfunction. SOD1 level is mainly regulated in response to oxidative stress, and long-term activation of SOD1 may lead to accumulation of aggregated SOD1 in the cytoplasm [55] . These inclusions may be linked to their fragmented mitochondrial network, seen in this cell line.

HEK293 cells exhibited the highest extranuclear TDP-43 signal, localized to the perinuclear region without detectable aggregation. For aSyn, EGFP-tagged and untagged overexpression systems yielded distinct localization patterns across cell lines: EGFP-aSyn showed higher cytoplasmic localization in HEK293 and SH-SY5Y compared to H4 cells, while untagged aSyn produced significantly higher nuclear localization specifically in SH-SY5Y cells. These differences may reflect the chromosome 4 triplication in H4 cells, tag-dependent effects, or cell line-specific proteostatic and cytoskeletal contexts. Additional experiments are needed to distinguish between these possibilities.

Collectively, this systematic characterization demonstrates that HEK293, H4, and SH-SY5Y cells differ substantially in cytoskeletal architecture, organelle morphology, protein quality control engagement, and the subcellular distribution of disease-relevant proteins. These differences are not independent but form coherent, cell line-specific biological identities shaped by their genetic backgrounds. Understanding this biological context is

therefore essential for correctly designing experiments, interpreting results, and selecting the most appropriate cell line model for research.

Methods

Cell culture

H4, HEK293, and SH-SY5Y cells (Sigma-Aldrich; © Merck KGaA, Darmstadt, Germany) were grown according to standard protocols; H4 in Opti-MEM Reduced Serum Medium, GlutaMAX ® supplement (Cat No. 51985026, Gibco®), supplemented with 10 % (v/v) fetal calf serum (FCS) (Cat No. AC-SM-0033, Anprotec) and 1 % (v/v) penicillin/streptomycin (pen/strep) (Cat No. MS01DF1009, Anprotec); HEK293 cells in Dulbecco's Modified Eagle's Medium High Glucose (DMEM) (Cat No. AC-LM-0014, Anprotec), supplemented with 10 % (v/v) FCS and 1 % (v/v) pen/strep; and SH-SY5Y cells in DMEM supplemented with 10 % (v/v) FCS, 1 % (v/v) pen/strep, and 1% MEM Non-essential amino acids (Cat No. 11140050, Gibco ®). The cells were maintained at 37 °C in a humidified atmosphere containing 5 % CO_2 under standard cell culture conditions. For all experiments, cells were plated when cultures reached approximately 70-80 % confluence. Cells were seeded at a density of ~80,000 cells per well in 12-well plates with crystal coverslips and allowed to adhere for 24 h prior to transfection or downstream analyses.

Karyotyping

Cell cultures were treated with Colcemide solution (10 µg/ml; Sigma-Aldrich) for 30 min at 37 °C. Cells were detached with accutase (Thermo Fisher) for 1 min at 37 °C collected

in a 15 mL tube and centrifuged at 200g, 5 min (RT). The supernatant was discarded, and the cell pellet resuspended in 1 mL culture medium by tapping the tube carefully. Pre-warmed (37 °C) hypotonic KCl/sodium citrate solution (1/1, 0.075 M/3.8 mM) was added dropwise to the cell suspension while shaking the tube carefully (approx. 8 mL). After 15 min of incubation at 37 °C, the cells were centrifuged (1000 rpm, 8 min (RT)) and the supernatant discarded. Pre-cooled (−20 °C) fixative (3:1 methanol/glacial acetic acid v/v) was then added dropwise to the cell suspension while shaking the tube carefully. The cells were incubated on ice for 10 min and then centrifuged (fixation and centrifugation steps were repeated three times). Fixed cells were dropped onto slides and baked at 60 °C overnight. Dry samples were immersed in 0.15 % trypsin/NaCl (Biochrom) for 50–60 s and stained with 5 % Giemsa (Merck). A total of 11 G-banded metaphases were analyzed from the selected cell lines. Karyotypes were arranged using the IKAROS imaging system (Metasystems).

Cell transfections

Cells were transfected using reagents optimized for each cell line with the following plasmids (pcDNA3.1+): SOD1 WT, SOD1 A4V, TDP43-Tomato, alpha-synuclein-EGFP (aSyn-EGFP), untagged alpha-synuclein (aSyn), and LRRK2. On the day of transfection, culture medium was replaced with fresh complete medium. Transfection complexes were prepared in Opti-MEM without additives according to the manufacturer's recommendations.

Briefly, for H4 cells, transfection was performed using FuGENE® HD Transfection Reagent (Cat No. E2312, Promega) and 2 µg of DNA (1:3 DNA-to-reagent ratio). The

reagent and DNA were incubated for 30 min at room temperature to allow complex formation and was added in a dropwise fashion to each well.

For HEK293 cells, transfection was carried out using Metafectene (Cat No. T020, Biontex). DNA and reagents were first diluted separately in Opti-MEM without additives and pre-incubated for 5 min at room temperature. Metafectene was used at a DNA-to-reagent ratio of 1:3. The solutions were then combined, incubated for 20 min at room temperature, and added in a dropwise fashion to the cells.

For SH-SY5Y cells, transfection was performed using Lipofectamine 3000 (Cat No. 100022052, Invitrogen) in combination with P3000 reagent (Cat No. 100022058, Invitrogen). P3000 reagent was diluted in Opti-MEM and 2 ug of plasmid DNA were added. Lipofectamine was diluted separately in Opti-MEM. After 5 min incubation at room temperature, both solutions were combined and incubated for 15 min at room temperature to allow complex formation. The mixture was added in a dropwise fashion to the cells.

Cells were maintained 48 h after transfection under standard culture conditions and processed for downstream analyses.

Starvation assay

Cells were plated in 12-well plates and cultured in complete growth medium for 24 h. The medium was then replaced with either Earle's Balanced Salt Solution (EBSS; Gibco) to induce starvation or complete growth medium as a non-starved control. Cells were maintained under starvation conditions for 3, 6, or 24 h before harvest for Western blot analysis.

Western blot

Cells were lysed in RIPA buffer (50 mM Tris-HCl, pH 8.0; 150 mM NaCl; 0.1% SDS; 1% NP-40; 0.5% sodium deoxycholate; 2 mM EDTA) supplemented with protease and phosphatase inhibitors for 30 min on ice. Protein concentration was determined, and 30 µg of total protein was denatured in 5× loading buffer and separated on a 12% SDS-PAGE gel. Proteins were transferred to nitrocellulose membranes using iBlot 2 transfer system at 20 V for 7 minutes. Membranes were blocked in 5% BSA in TBS-T for 1 h at room temperature and incubated with primary antibodies mouse alpha tubulin (Cat no T9020, Sigma), mouse Acetylated tubulin (Cat No T7451, Sigma), mouse Beta actin (Cat no A5441, Sigma), rabbit TIA1 (Cat no sc166247, Santa Cruz Biotechnology), rabbit TOM20 (Cat no 424065, Cell Signaling), rabbit vinculin (Cat no 13901S, Cell Signaling), rabbit GAPDH (Cat no 2118S, Cell signaling), mouse ubiquitin (Cat no 3936, Cell signaling), rabbit S6 (Cat no 2217, cell signaling), rabbit pS6 (Cat no 4858T, cell signaling), rabbit LC3 (Cat no PA1-46286, Invitrogen), rabbit LAMP1 (Cat no ab24170, Abcam), rabbit p62 (Cat no ab91526, abcam) , and mouse G3BP (Cat no 611126, BD Biosciences) overnight at 4 °C. After washing, membranes were incubated with HRP-conjugated secondary antibodies (anti-mouse or anti-rabbit (Amersham)) for 1 h at room temperature. Signal was revealed using the Immobilon Western chemiluminescent HRP-substrate (Cat No. WBKLS0050, EMD Millipore) and detected using the Fusion FX (Vilber). Densitometric analyses of the bands were performed using FIJI® software (NIH).

Immunocytochemistry

After the cells reached the desired confluence, the cell culture media was removed, and cells were washed three times with PBS. Then, the cells were fixed with ice-cold PFA 4% for 10 min and washed three times with PBS for 5 min with gentle shaking. Afterwards,

cells were permeabilized with PBS/Triton 0.1% for 10 min at RT. The cells were washed once with PBS for 5 min and incubated in a blocking solution (PBS/BSA 3%) with gentle shaking for 1 h at RT. Next, cells were incubated at with gentle shaking at 4 °C overnight with the following antibodies: anti-Calnexin (Cat No. ab22595, Abcam), anti-GM130 [EP892Y] (Cat No. ab302489, Abcam), anti-α-Synuclein (Cat No. 610787, BD biosciences), rabbit LC3 (Cat no PA1-46286, Invitrogen), anti-SOD1 (UbetaB) (Cat No. SPC-205, Stress Marq Biosciences Inc.), rabbit V5 (Cat No. ab9116, Abcam), rabbit TOM20 (Cat no 424065, Cell Signaling), mouse Lamp1 (Cat No. sc-20011,Santa Cruz), mouse alpha tubulin (Cat No. T9020, Sigma), mouse Acetylated tubulin (Cat No. T7451, Sigma), mouse Beta actin (Cat No. A5441, Sigma), and rabbit alpha tubulin (Cat No. 302217, SYSY antibodies). Then, the cells were washed three times with PBS, 5 min each wash, and were incubated with the secondary antibodies for 2 h at RT. The cells were protected from the light. Immediately, nuclei were stained with DAPI (0.2 µg/µL) for 10 min at RT and mild shaking. Cells were washed three times with PBS and mounted on a slide with a Fluoromount-G (Cat No. 00-4958-02, Invitrogen). Negative controls were performed excluding the primary antibodies from the procedure.

Microscopy and image acquisition

Confocal images were acquired using a Zeiss LSM900 confocal microscope with Airyscan super-resolution detection and a 63x oil immersion objective (NA 1.4). Digital images were acquired using the Zen Blue 3.4 software (Zeiss). At least 30 cells per biological replicate were randomly selected per cell line to be imaged. Z-stacks comprised 5 optical sections per cell, spanning from one edge to the other of each cell to encompass the cellular volume (approximately 2 µm total depth, 0.4-0.5 µm z-step interval).

Mitochondrial morphology analysis

Immunofluorescence staining of TOM20 was performed in HEK293, H4 and SHSY5Y cells, followed by quantitative image analysis in Fiji/ImageJ (National Institutes of Health) and quantification of the mitochondrial area. Images were collected under the same acquisition conditions to enable a direct comparison of mitochondrial features under different conditions for all three cell lines. Only cells with clear TOM20 staining with little overlap with neighboring cells were analyzed. To accentuate mitochondria and minimize noise, raw TOM20 images were first converted to 8-bit in Fiji and further proceeded for background subtraction and edge/contrast enhancement. Images were then thresholded using an automatic global thresholding algorithm to create a binary mask of the mitochondrial compartment, and small objects and debris were removed with the "Analyze Particles" minimum size filter with a cutoff 0.2 μm^2. The geometric parameters of the mitochondria, such as area and perimeter, were calculated per mitochondrion from the resulting binary mask using the ImageJ "Analyze Particles" tool, and the average per cell was calculated to get a mean mitochondrial area and mean mitochondrial perimeter. The mean mitochondrial form factor was calculated using the following equation "area"/(4π×"perimeter"). The binarized TOM20 masks were skeletonized using the "Skeletonize" algorithm and network parameters were extracted with the "Analyze Skeleton (2D/3D)" plug-in. The number of branches and number of branches per mitochondrion for each cell were determined by calculating the total number of branches for each mitochondrial network, and then dividing it by the number of individual mitochondrial objects that were found within the network in the binary cell mask. The mean mitochondrial branch length was determined as the mean length of all branches of

the skeletonized cells' mitochondrial network. In each cell line, these parameters (mean mitochondrial area, mean perimeter, mean form factor, total branches, branches per mitochondrion and mean branch length) were calculated per cell, and then averaged across several cells and used to form distributions with which to compare the various cell lines.

Image processing and segmentation

Image analysis to quantify aSyn distribution, TDP43 distribution, and the morphology of the Golgi apparatus and the ER was performed using Python 3.13.9 within a Conda virtual environment on Windows 11 using Jupyter Notebooks. Custom scripts utilized the following key libraries: NumPy (v2.2.5) for numerical array operations, scikit-image (v0.25.2) for image segmentation and morphological operations, Cellpose for deep learning-based segmentation (Stringer et al., 2021) (v4.0.8), and Pandas (v3.0.0) for data aggregation and analysis, and Matplotlib (v3.10.5) and Seaborn (v.0.13.2) for initial data visualization. Maximum intensity projections (MIPs) were generated from 3D Z-stacks for each channel using the czifile package (v.2019.7.2.1).

aSyn distribution quantification

Image analysis was performed using Python 3.13.9 and a custom script processed the files. First, nuclei were segmented with Cellpose using the "nuclei" model with a diameter of 80 pixels, while whole cells were segmented using the "cyto2" model with a diameter of 150 pixels. Small objects, less than 100 pixels for nuclei and 150 for cells, were removed using scikit-image's remove small objects function. Masks were saved as 3D NumPy arrays for each image. For intensity quantification, images were loaded using

czifile, and the target channel was extracted. Thresholding was applied using Otsu's method (from scikit-image) to separate foreground signal from background, with a channel-specific multiplier (0.3 for 488 nm, 0.7 for 633 nm) to optimize noise reduction. Pixels below the threshold were set to zero. Per-cell analysis was conducted by isolating each cell mask and its overlapping nucleus. Mean intensities were calculated in the nucleus and cytoplasm (cell minus nucleus) using the thresholded signal. Then, percentages were computed as nucleus mean / (nucleus mean + cytoplasm mean) * 100 for nucleus % (cytoplasm % = 100 - nucleus %). Cells with zero total mean intensity were excluded which are the non-transfected cells.

Golgi apparatus segmentation and morphology measurements

Image analysis was performed using Python 3.13.9 and a custom script processed the files. First, MIPs were generated from the z-stacks using the czifile library. The Golgi apparatus MIP was processed with a multi-scale Gaussian smoothing approach (sigmas = 0.5, 1.0, 1.5, 2.0), followed by Otsu thresholding for each scale and intensity enhancement to isolate bright ribbon structures. A combined response map was created by averaging the enhanced images, thresholded with Otsu, and segmented using distance-transform watershed to label individual fragments. Next, based on centroid distance, the fragments within 3.5 μm were merged into complete ribbons using a union-find algorithm. Nuclei were segmented using Gaussian smoothing (sigma = 1.0) followed by Otsu thresholding to generate a binary mask. The mask was cleaned with morphological opening (disk radius = 2) and removal of small objects (minimum size = 100 pixels) using scikit-image. The resulting binary mask was labeled to identify individual nuclei. Merged Golgi ribbons were assigned to the nearest nucleus based on centroid

distance, calculated using a k-d tree from SciPy's cKDTree. For each merged and assigned Golgi apparatus, area (in μm²) and perimeter were calculated using scikit-image's regionprops. Compactness was computed as 4π * area / perimeter² (unitless, ranging from 0 for dispersed shapes to 1 for compact circles). Ribbon length (in μm) was measured by skeletonizing each merged mask to a 1-pixel-wide backbone and summing the pixels, scaled by pixel size. Initial visualization was generated using Seaborn and Matplotlib.

Endoplasmic reticulum segmentation and morphology measurements

Image analysis was performed using Python 3.13.9 and a custom script processed the files. To quantify the ER morphology, MIPs were generated from the z-stacks using the czifile library. Nucleus MIPs were segmented using scikit-image. The image was smoothed with a Gaussian filter (sigma = 1.0), thresholded with Otsu's method, cleaned with morphological opening (disk radius = 2), and small objects removed (minimum size = 100 pixels). The resulting binary mask was labeled to identify individual nuclei. Cell boundaries were segmented from the ER MIP with Cellpose using the “cyto2” model (diameter=250). The ER MIP was smoothed with a Gaussian filter (sigma=1.5) and normalized to uint8. Dual-channel input was used to use the nucleus as anchor. The segmented mask was cleaned with the remove small objects (minimum size = 5000) function and labeled. For each labeled cell, concentric rings (zones) were created by normalizing distances from the nucleus boundary to the cell edge using distance transform edt from scipy.ndimage. The ER was divided into 4 equal radial bins, excluding the nucleus. For each zone, mean intensity was calculated from the ER MIP in the ring

mask. Area was calculated as pixel count in the ring mask, converted to μm². Initial visualization was generated using Seaborn and Matplotlib.

TDP43 characterization and quantification

Image analysis was performed using Python 3.13.9 and a custom script processed the files. To focus on transfected cells, regions of interest (ROIs) were detected from the TDP43-tdTomato channel. The tomato channel was smoothed with a Gaussian filter (sigma = 1.0), and Otsu thresholding was applied to create a binary mask of active regions. Small objects were removed (minimum size = 200 pixels). Blobs were labeled and filtered by cell-line-specific area ranges (HEK293: 20,000–90,000 pixels; H4: 20,000–70,000; SH-SY5Y: 20,000–60,000) and solidity (0.65–0.95). Filtered blobs were dilated (disk radius = 20 pixels) to create ROIs capturing potential perinuclear signal that could be confused with cytoplasmic signal. For each ROI crop, the nucleus was defined by Otsu thresholding on the DAPI crop, multiplied by a factor of 0.5 for optimal boundary detection. TDP43-tdTomato signal was measured as mean intensity inside the nuclear mask (nuclear localization) and outside it (cytoplasmic localization). The percentage outside was calculated as (outside sum / total sum) × 100. The nuclear/cytoplasmic ratio was computed as nuclear mean / cytoplasmic mean. Initial visualization was generated using Seaborn and Matplotlib.

Statistical Analysis

Statistical analysis was performed in GraphPad Prism. Multiple-group comparisons were performed using ANOVA followed with Tukey´s multiple comparisons test. $p < 0.05$ was considered statistically significant (* $p < 0.05$; ** $p < 0.001$; *** $p < 0.0001$).

Acknowledgments: TFO is supported by the Deutsche Forschungsgemeinschaft (DFG, German Research Foundation) under Germany's Excellence Strategy – EXC 2067/1-390729940, and SFB1286 (Project B8). MM is supported by DAAD Research Grants - Doctoral Programmes in Germany, 57552340. MFL is supported by the Alexander von Humboldt Foundation. VSB is supported by a fellowship from Coordenação de Aperfeiçoamento de Pessoal de Nível Superior (CAPES, process n°. 88887.169657/2025-00).

Authors' Roles: TFO conceived the study, analyzed data. MFL, MM, TA, VSB, IE performed experiments and analyzed the data. All authors wrote and revised the manuscript.

Financial disclosure/Conflict of Interest: The authors declare no conflicts of interest.

Funding: TFO is supported by the Deutsche Forschungsgemeinschaft (DFG, German Research Foundation) under Germany's Excellence Strategy – EXC 2067/1-390729940, and SFB1286 (Project B8). M.M. is supported by DAAD Research Grants - Doctoral Programmes in Germany, 57552340. M.F.L. is supported by the Alexander von Humboldt

Foundation. V.S.B VSB is supported by a fellowship from Coordenação de Aperfeiçoamento de Pessoal de Nível Superior (CAPES, process n°. 88887.169657/2025-00).

Code availability statement: Custom python scripts used for ER and Golgi morphology and aSyn and TDP43 localization analyses are available as Jupyter notebooks at “https://gitlab.gwdg.de/cell_comparison_review/cell_models_comparison.git”. Upon acceptance, the code will be permanently archived at Zenodo under DOI: 10.5281/zenodo.21127442.

References

1. He, Z. *et al.* Chromosomal instability and its effect on cell lines. *Cancer Rep.* **6**, (2023).
2. Tosh, J., Tybulewicz, V. & Fisher, E. M. C. Mouse models of aneuploidy to understand chromosome disorders. *Mammalian Genome* **33**, 157–168 (2022).
3. Hwang, S. *et al.* Consequences of aneuploidy in human fibroblasts with trisomy 21. *Proceedings of the National Academy of Sciences* **118**, (2021).
4. Sheltzer, J. M., Torres, E. M., Dunham, M. J. & Amon, A. Transcriptional consequences of aneuploidy. *Proceedings of the National Academy of Sciences* **109**, 12644–12649 (2012).
5. Shepherd, C. E., Yang, Y. & Halliday, G. M. Region- and Cell-specific Aneuploidy in Brain Aging and Neurodegeneration. *Neuroscience* **374**, 326–334 (2018).
6. Hwang, S. *et al.* Consequences of aneuploidy in human fibroblasts with trisomy 21. *Proceedings of the National Academy of Sciences* **118**, (2021).
7. Potter, H. *et al.* Chromosome Instability and Mosaic Aneuploidy in Neurodegenerative and Neurodevelopmental Disorders. *Front. Genet.* **10**, (2019).
8. Singleton, A. B. *et al.* α-Synuclein Locus Triplication Causes Parkinson's Disease. *Science (1979).* **302**, 841–841 (2003).
9. Ahn, T.-B. *et al.* α-Synuclein gene duplication is present in sporadic Parkinson disease. *Neurology* **70**, 43–49 (2008).
10. Landoulsi, Z. *et al.* Large-scale copy number variant analysis in genes linked to Parkinson´s disease. *NPJ Parkinsons Dis.* **11**, 225 (2025).
11. Oromendia, A. B. & Amon, A. Aneuploidy: implications for protein homeostasis and disease. *Dis. Model. Mech.* **7**, 15–20 (2014).
12. Veitia, R. A., Bottani, S. & Birchler, J. A. Cellular reactions to gene dosage imbalance: genomic, transcriptomic and proteomic effects. *Trends in Genetics* **24**, 390–397 (2008).
13. Smethurst, P. *et al.* Distinct responses of neurons and astrocytes to TDP-43 proteinopathy in amyotrophic lateral sclerosis. *Brain* **143**, 430–440 (2020).
14. Geibl, F. F. *et al.* Mapping cellular vulnerability in Parkinson's disease using retro-AAVs and preformed α-synuclein fibrils. *Transl. Neurodegener.* **15**, 2 (2026).
15. Gimón, I. V, Sandefur, C. & Schnell, S. Macromolecular crowding and protein aggregation: Friend, foe or contextual force? *Prog. Biophys. Mol. Biol.* **199**, 79–98 (2026).
16. Mofrad, M. R. K. Rheology of the Cytoskeleton. *Annu. Rev. Fluid Mech.* **41**, 433–453 (2009).

17. Hohmann, T. & Dehghani, F. The Cytoskeleton—A Complex Interacting Meshwork. *Cells* **8**, 362 (2019).
18. Gidalevitz, T., Prahlad, V. & Morimoto, R. I. The Stress of Protein Misfolding: From Single Cells to Multicellular Organisms. *Cold Spring Harb. Perspect. Biol.* **3**, a009704 (2011).
19. Sahoo, S., Padhy, A. A., Kumari, V. & Mishra, P. Role of Ubiquitin–Proteasome and Autophagy-Lysosome Pathways in α-Synuclein Aggregate Clearance. *Mol. Neurobiol.* **59**, 5379–5407 (2022).
20. Yuan, L. *et al.* Stress granules: emerging players in neurodegenerative diseases. *Transl. Neurodegener.* **14**, 22 (2025).
21. Tolosa, E., Vila, M., Klein, C. & Rascol, O. LRRK2 in Parkinson disease: challenges of clinical trials. *Nat. Rev. Neurol.* **16**, 97–107 (2020).
22. Jo, M. *et al.* The role of TDP-43 propagation in neurodegenerative diseases: integrating insights from clinical and experimental studies. *Exp. Mol. Med.* **52**, 1652–1662 (2020).
23. Lundin, V. F., Leroux, M. R. & Stirling, P. C. Quality control of cytoskeletal proteins and human disease. *Trends Biochem. Sci.* **35**, 288–297 (2010).
24. Gasic, I. & Mitchison, T. J. Autoregulation and repair in microtubule homeostasis. *Curr. Opin. Cell Biol.* **56**, 80–87 (2019).
25. Gasic, I., Boswell, S. A. & Mitchison, T. J. Tubulin mRNA stability is sensitive to change in microtubule dynamics caused by multiple physiological and toxic cues. *PLoS Biol.* **17**, e3000225- (2019).
26. Lucas, L. *et al.* Tubulin transforms Tau and α-synuclein condensates from pathological to physiological. *Nat. Commun.* **17**, 3362 (2026).
27. Eshun-Wilson, L. *et al.* Effects of α-tubulin acetylation on microtubule structure and stability. *Proceedings of the National Academy of Sciences* **116**, 10366–10371 (2019).
28. Portran, D., Schaedel, L., Xu, Z., Théry, M. & Nachury, M. V. Tubulin acetylation protects long-lived microtubules against mechanical ageing. *Nat. Cell Biol.* **19**, 391–398 (2017).
29. Donker, L. & Godinho, S. A. Rethinking tubulin acetylation: From regulation to cellular adaptation. *Curr. Opin. Cell Biol.* **94**, 102512 (2025).
30. Weissman, A. M. Themes and variations on ubiquitylation. *Nat. Rev. Mol. Cell Biol.* **2**, 169–178 (2001).
31. Weissman, A. M., Shabek, N. & Ciechanover, A. The predator becomes the prey: regulating the ubiquitin system by ubiquitylation and degradation. *Nat. Rev. Mol. Cell Biol.* **12**, 605–620 (2011).
32. Rabanal-Ruiz, Y., Otten, E. G. & Korolchuk, V. I. mTORC1 as the main gateway to autophagy. *Essays Biochem.* **61**, 565–584 (2017).

33. Kim, Y. C. & Guan, K.-L. mTOR: a pharmacologic target for autophagy regulation. *J. Clin. Invest.* **125**, 25–32 (2015).
34. Li, X.-J., Orr, A. L. & Li, S. Impaired mitochondrial trafficking in Huntington's disease. *Biochimica et Biophysica Acta (BBA) - Molecular Basis of Disease* **1802**, 62–65 (2010).
35. Kang, D. E. *et al.* The Interface between Cytoskeletal Aberrations and Mitochondrial Dysfunction in Alzheimer's Disease and Related Disorders. *Exp. Neurobiol.* **20**, 67–80 (2011).
36. Klemmensen, M. M., Borrowman, S. H., Pearce, C., Pyles, B. & Chandra, B. Mitochondrial dysfunction in neurodegenerative disorders. *Neurotherapeutics* **21**, (2024).
37. Hou, Y. *et al.* Urolithin A improves Alzheimer's disease cognition and restores mitophagy and lysosomal functions. *Alzheimer's & Dementia* **20**, 4212–4233 (2024).
38. Frey, T. G. & Mannella, C. A. The internal structure of mitochondria. *Trends Biochem. Sci.* **25**, 319–324 (2000).
39. Illescas, M., Peñas, A., Arenas, J., Martín, M. A. & Ugalde, C. Regulation of Mitochondrial Function by the Actin Cytoskeleton. *Front. Cell Dev. Biol.* **Volume 9-2021**, (2021).
40. Yadav, T., Gau, D. & Roy, P. Mitochondria–actin cytoskeleton crosstalk in cell migration. *J. Cell. Physiol.* **237**, 2387–2403 (2022).
41. Fernández Casafuz, A. B., De Rossi, M. C. & Bruno, L. Mitochondrial cellular organization and shape fluctuations are differentially modulated by cytoskeletal networks. *Sci. Rep.* **13**, 4065 (2023).
42. Moore, A. S., Wong, Y. C., Simpson, C. L. & Holzbaur, E. L. F. Dynamic actin cycling through mitochondrial subpopulations locally regulates the fission–fusion balance within mitochondrial networks. *Nat. Commun.* **7**, 12886 (2016).
43. Zhao, Q., Zhang, Z.-R., Ye, Y. & Liu, Y. Endoplasmic reticulum (ER) ubiquitin ligases: substrate recognition and emerging cellular functions. *Trends Cell Biol.* https://doi.org/10.1016/j.tcb.2026.04.004 (2026) doi:10.1016/j.tcb.2026.04.004.
44. Lemanowicz, J. *et al.* Biochemical Mechanisms of Cellular Stress Adaptation in the Pathogenesis of Chronic Diseases. *Molecules* **31**, 1381 (2026).
45. Benyamini, P. & Meyer, D. I. ER biogenesis without stress: how the ribosome receptor, p180, defines a developmental program beyond the UPR. *Front. Cell Dev. Biol.* **13**, (2025).
46. Abaandou, L., Quan, D. & Shiloach, J. Affecting HEK293 Cell Growth and Production Performance by Modifying the Expression of Specific Genes. *Cells* **10**, 1667 (2021).
47. Malm, M. *et al.* Harnessing secretory pathway differences between HEK293 and CHO to rescue production of difficult to express proteins. *Metab. Eng.* **72**, 171–187 (2022).

48. İŞLEK CAMADAN, E. E., SARIHAN, M., KASAP, M., AKPINAR, G. & KOÇYİĞİT, E. Evaluating SH-SY5Y cells as a dopaminergic neuronal model: morphological, transcriptomic, and proteomic insights. *Turkish Journal of Biology* **49**, 700–711 (2025).
49. Filograna, R. *et al.* Analysis of the Catecholaminergic Phenotype in Human SH-SY5Y and BE(2)-M17 Neuroblastoma Cell Lines upon Differentiation. *PLoS One* **10**, e0136769 (2015).
50. Huttunen, H. J. *et al.* Inhibition of acyl-coenzyme A: cholesterol acyl transferase modulates amyloid precursor protein trafficking in the early secretory pathway. *The FASEB Journal* **23**, 3819–3828 (2009).
51. Bustamante, H. A. *et al.* Turnover of C99 is Controlled by a Crosstalk between ERAD and Ubiquitin-Independent Lysosomal Degradation in Human Neuroglioma Cells. *PLoS One* **8**, e83096 (2013).
52. Deniston, C. K. *et al.* Structure of LRRK2 in Parkinson's disease and model for microtubule interaction. *Nature* **588**, 344–349 (2020).
53. Kett, L. R. *et al.* LRRK2 Parkinson disease mutations enhance its microtubule association. *Hum. Mol. Genet.* **21**, 890–899 (2012).
54. Leschziner, A. E. & Reck-Peterson, S. L. Structural Biology of LRRK2 and its Interaction with Microtubules. *Movement Disorders* **36**, 2494–2504 (2021).
55. Monteiro Neto, J. R. *et al.* SOD1, A Crucial Protein for Neural Biochemistry: Dysfunction and Risk of Amyotrophic Lateral Sclerosis. *Mol. Neurobiol.* **62**, 14966–14986 (2025).

Figure legends

Figure 1. Karyotype analysis. Representative metaphase spread following G-banding and karyotype analysis, indicating the modal number of chromosomes of A. HEK293, B. H4, C. SH-SY5Y cells.

Figure 2. Cell morphology and the difference in cytoskeletal architecture in the different cells. A. Representative confocal images showing the cytoskeletal architecture of HEK293, H4 and SH-SY5Y (microtubules in green (alpha-tubulin), actin filaments in red (beta-actin), and the nucleus in blue). B. Cell and nucleus size analysis of the different cell lines (1-way ANOVA; Tukey´s multiple comparisons test, *** p=0.0001, **** p<0.0001; at least 20 cells per group were analyzed). C. Representative confocal images showing the acetylated tubulin in HEK293, H4, and SH-SY5Y (acetylated tubulin in pink, and the nucleus in blue). D. Representative western blots showing the levels of cytoskeletal

markers across the cell lines. E. Quantification of D (N=3, 1-way ANOVA; Tukey´s multiple comparisons test, * p<0.05, ** p =0,0055).

Figure 3. Autophagy markers in the different cell lines. A. Representative confocal images showing the different autophagic markers in HEK293, H4, and SH-SY5Y cells (LC3 in green, LAMP1 in yellow, Lysotracker in pink, and the nucleus in blue). B. Lysosomal acidity analysis in the different cell lines (1-way ANOVA; Tukey´s multiple comparisons test, *** p=0,0006, **** p<0.0001; at least 20 cells per group were analysed). C. Representative western blot from LC3I and LC3II. D. Quantification of LC3I and LC3II represented as a ratio between both proteins (N=3, 1-way ANOVA; Tukey´s multiple comparisons test). E. Representative western blot of the lysosomal marker Lamp1 across different cell lines. F. Quantification of E (N=3, 1-way ANOVA; Tukey´s multiple comparisons test). G. Representative western blot showing the typical ubiquitin signal in the different cell lines.

Fig 4. Starvation kinetics across different cell lines. A. Representative western blot showing the effect of starvation for 3,6 and 24 hours on the mTOR effector S6 and its phosphorylated form (P-S6), and the p62, the autophagosome marker in HEK293T cells. B. Quantification of A. (N=3). C. Representative western blot showing the effect of starvation for 3,6 and 24 hours on S6, P-S6, and p62 in H4 cells. D. Quantification of C. (N=3). E. Representative western blot showing the effect of starvation for 3,6 and 24 hours on S6, P-S6, and p62 in SH-SY5Y cells. F. Quantification of E.

Fig 5. Mitochondrial network across the cell lines. A. Representative confocal images of the mitochondria in HEK293, H4, and SH-SY5Y cells (TOM20 in red, nucleus in blue).

B. Representative western blot showing the level of TOM20 in the cell lines. C. Quantification of the protein content in B (N=3, 1-way ANOVA; Tukey´s multiple comparisons test, * p=0,0435) D - I. Quantification of mitochondrial parameters from A.

Fig 6. Differences in endoplasmic reticulum morphology across the cell lines. A. Top row: representative confocal images of the ER (calnexin in green) of HEK293, H4 and SH-SY5Y. Bottom row: ER mask segmentation showing the 4 zones. B. The intensity fluorescence per zone. The intensity fluorescence decreases progressively for all the cell lines as the ER reaches the periphery. The intensity in each zone differs significantly among all the cell lines. C. Area (µm2) of the ER has per zone. The zone area is significantly different among all the cell lines. HEK293 cells have the smallest area, followed by SH-SY5Y, and H4. ***P<0.001, 1-way ANOVA; Tukey´s multiple comparisons test. N= at least 100 cells from 3 biological replicates.

Fig 7. Differences in Golgi apparatus morphology across the cell lines. A. Top row: representative images in grayscale showing the normalized image; colorful overlay represents the segmentation mask (Golgi regions in distinct spectral colors assigned to the corresponding cell). The white square marks the zoomed ROI depicted of HEK293, H4 and SH-SY5Y cells. The Bottom row: representative zoom confocal images of the ER (GM130 in red) in the ROI. B. Area of Golgi apparatus (µm2). HEK293 cells have the smallest area, followed by H4 and SH-SY5Y. Only the area of HEK293 cells is significantly different compared to H4 and SH-SY5Y. C. The compactness ratio of the Golgi apparatus. HEK293 cells have the most compact structure compared to H4 and SH-SY5Y. Nevertheless, only the comparison between HEK293 and SH-SY5Y is statistically

significant. D. The ribbon length of the Golgi apparatus (µm). HEK293 cells have the smallest ribbon length, followed by H4 and SH-SY5Y. Only the ribbon length of HEK293 cells is significantly different compared to H4 and SH-SY5Y. ***P<0.001, 1-way ANOVA; Tukey´s multiple comparisons test. N= at least 100 cells from 3 biological replicates.

Fig 8. The expression of LRRK2 in different cell lines. A. Representative confocal images showing the distribution of LRRK2 in different cell lines (LRRK2 in green, nucleus in blue). B. Quantification of LRRK2 filament structure in the different cell lines. C. Representative confocal images showing the colocalization of alpha-tubulin and LRRK2 in HEK293, H4, and SH-SY5Y (alpha-tubulin in pink, LRRK2 in green, and the nucleus in blue).

Fig 9. Differences in the localization of TDP43-tdTomato and the distribution of SOD1 WT and A4V across the cell lines. A. Representative confocal images of TDP43-tdTomato (red) in HEK293, H4 and SH-SY5Y. B. Representative analysis of regions of interest (ROI). RGB merge (TDP43-tdTomato in red, nuclei in blue) includes a white square marking the zoomed ROI depicted. Grayscale TDP43-tdTomato channel, binary threshold, and nuclear mask show variations in TDP43 localization patterns. C. The percentage of cells where the TDP43-tdTomato is detected outside of the nucleus. HEK293 cells have the highest percentage compared to H4 and SHSY5Y. ***P<0.001, 1-way ANOVA; Tukey´s multiple comparisons test. N = at least 70 cells from 3 biological replicates. D. Representative confocal images of SOD1 WT (green) in HEK293, H4 and SH-SY5Y. E. Representative confocal images of SOD1 A4V (green) in HEK293, H4 and SH-SY5Y. SOD1A4V-induced cytoplasmic inclusions in H4 cells. No inclusion-like structures were observed in HEK293 or SH-SY5Y cells. F. The percentage of HEK293,

H4 and SH-SY5Y cells with and without inclusions. N = at least 50 cells from 4 biological replicates.

Fig 10. Differences in aSyn across the cell lines. A. Representative confocal images of aSyn-EGFP in HEK293, H4 and SH-SY5Y (aSyn-EGFP, nucleus in blue). B. The distribution of aSyn-EGFP in the cytoplasm and in the nucleus. C. Representative confocal images of untagged aSyn in HEK293, H4 and SH-SY5Y (aSyn in red, nucleus in blue). D. The distribution of untagged aSyn in the cytoplasm and in the nucleus. Significant differences can be observed in the distribution among the three cell lines. ***P < 0.001, **P < 0.01, *P < 0.05** HEK293, H4 and SH-SY5Y at least 50 cells from 3 biological replicates.

Supplementary figure 1. Endoplasmic reticulum (ER) and Golgi apparatus. Representative confocal images showing the ER and the Golgi apparatus of HEK293, H4 and SH-SY5Y (calnexin in green for the ER, GM130 in red for the Golgi apparatus, and the nucleus in blue).

Supplementary figure 2. The difference in the stress granule in the different cell lines. A. Representative western blot showing the protein content of G3BP and TIA1 in different cell lines. B. Quantification of A (N=3, 1-way ANOVA; Tukey´s multiple comparisons test).

A.

HEK293

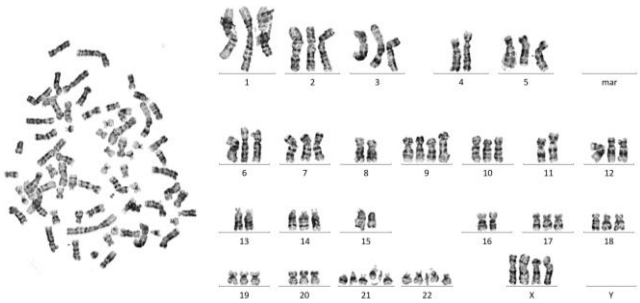

B.

H4

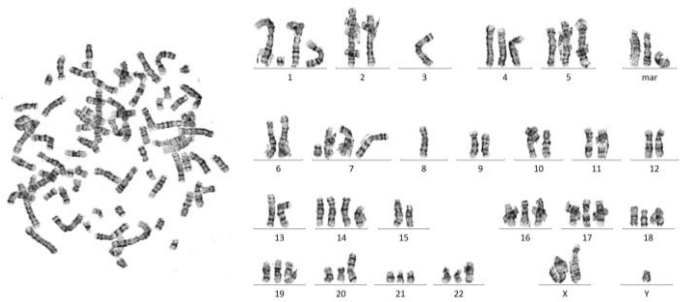

C.

SH-SY5Y

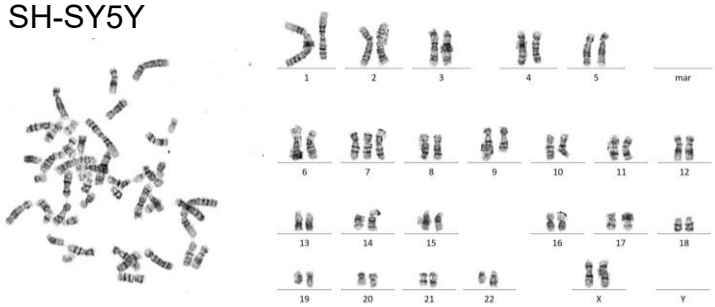

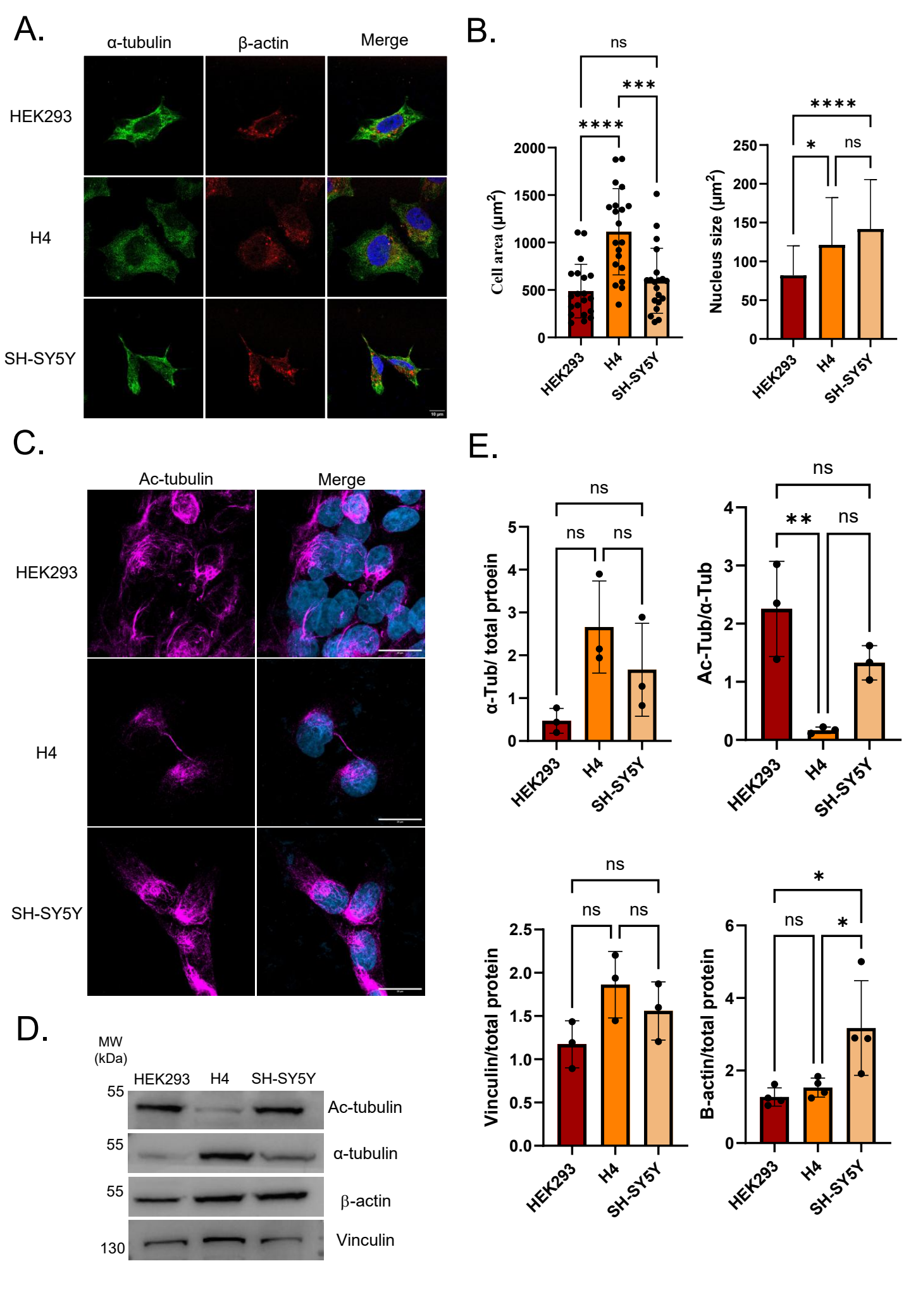
A.
α-tubulin
β-actin
Merge
HEK293
H4
SH-SY5Y
B.
ns
***
****
Cell area (μm²)
2000
1500
1000
500
0
HEK293
H4
SH-SY5Y
****
*
ns
Nucleus size (μm²)
250
200
150
100
50
0
HEK293
H4
SH-SY5Y
C.
Ac-tubulin
Merge
HEK293
H4
SH-SY5Y
E.
ns
ns
ns
α-Tub/ total prtoein
5
4
3
2
1
0
HEK293
H4
SH-SY5Y
ns
**
ns
Ac-Tub/α-Tub
4
3
2
1
0
HEK293
H4
SH-SY5Y
ns
ns
ns
Vinculin/total protein
2.5
2.0
1.5
1.0
0.5
0.0
HEK293
H4
SH-SY5Y
*
ns
*
B-actin/total protein
6
4
2
0
HEK293
H4
SH-SY5Y
D.
MW
(kDa)
HEK293
H4
SH-SY5Y
55
Ac-tubulin
55
α-tubulin
55
β-actin
130
Vinculin

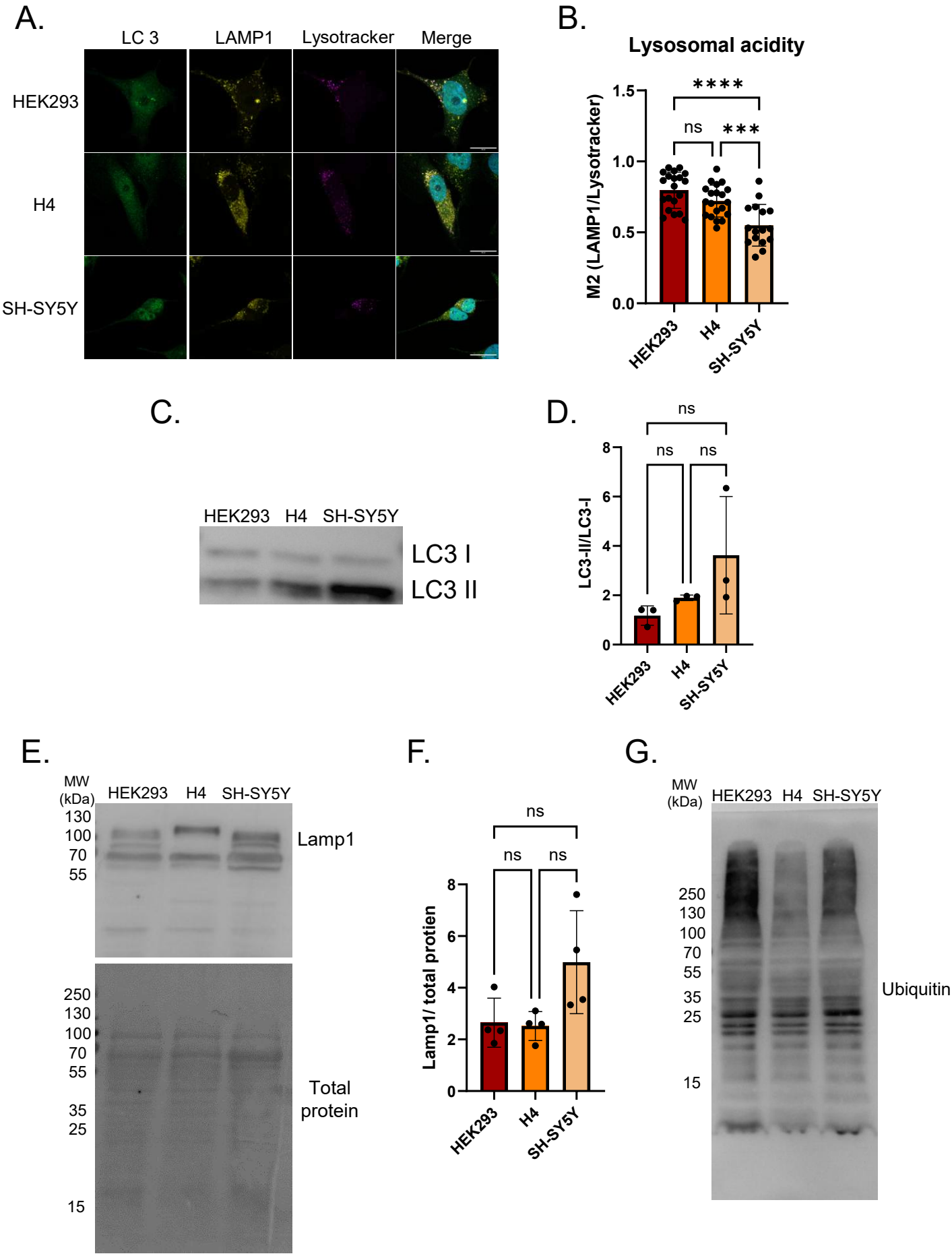
A.
LC 3
LAMP1
Lysotracker
Merge
HEK293
H4
SH-SY5Y
B.
Lysosomal acidity
M2 (LAMP1/Lysotracker)
****
ns
***
1.5
1.0
0.5
0.0
HEK293
H4
SH-SY5Y
C.
HEK293 H4 SH-SY5Y
LC3 I
LC3 II
D.
LC3-II/LC3-I
ns
ns
ns
8
6
4
2
0
HEK293
H4
SH-SY5Y
E.
MW (kDa)
HEK293 H4 SH-SY5Y
130
100
70
55
Lamp1
250
130
100
70
55
35
25
15
Total protein
F.
Lamp1/ total protien
ns
ns
ns
8
6
4
2
0
HEK293
H4
SH-SY5Y
G.
MW (kDa)
HEK293 H4 SH-SY5Y
250
130
100
70
55
35
25
15
Ubiquitin

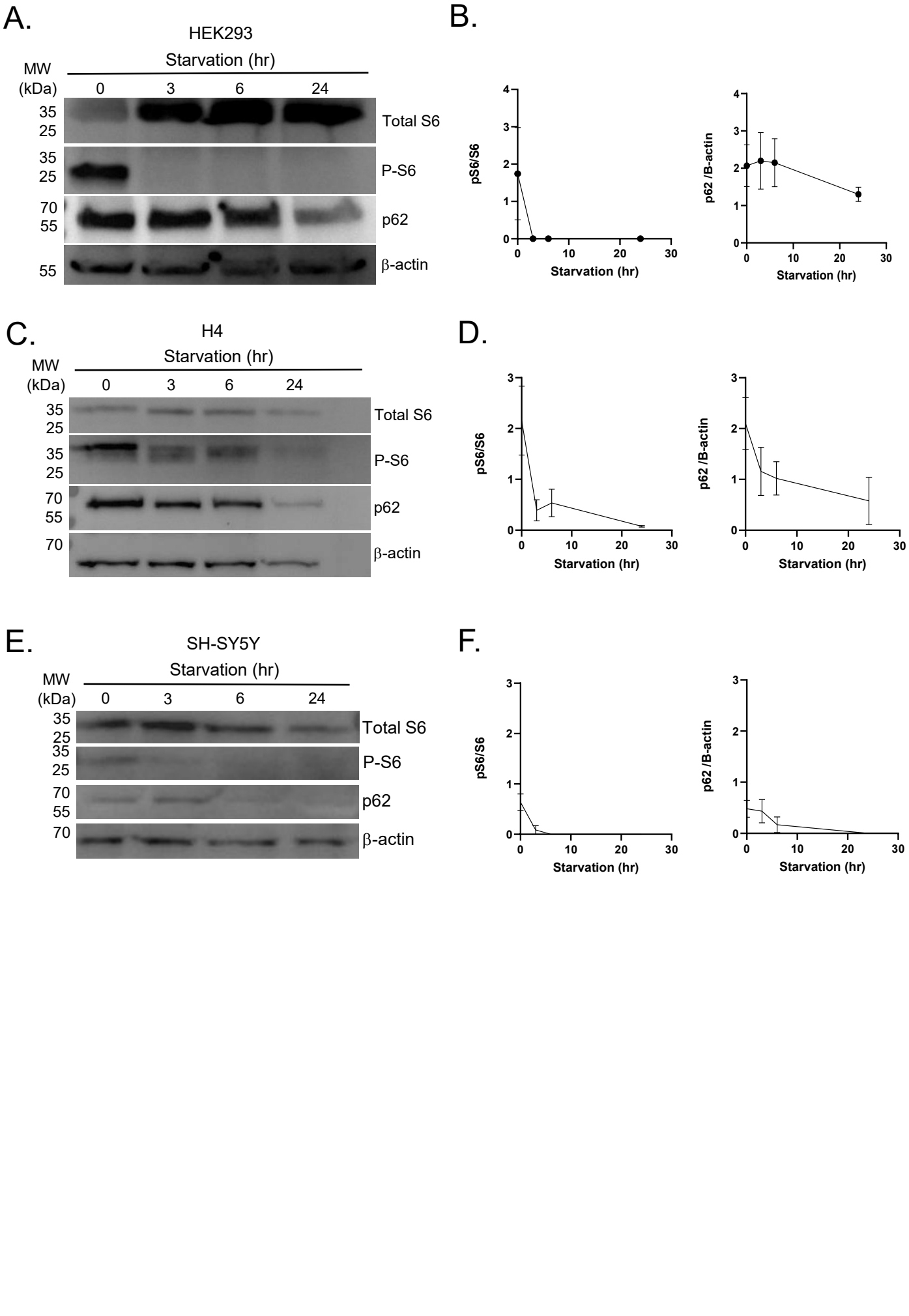
A.
HEK293
Starvation (hr)
MW
(kDa)
0
3
6
24
35
25
Total S6
35
25
P-S6
70
55
p62
55
β-actin
B.
pS6/S6
Starvation (hr)
p62 /B-actin
Starvation (hr)
C.
H4
Starvation (hr)
MW
(kDa)
0
3
6
24
35
25
Total S6
35
25
P-S6
70
55
p62
70
β-actin
D.
pS6/S6
Starvation (hr)
p62 /B-actin
Starvation (hr)
E.
SH-SY5Y
Starvation (hr)
MW
(kDa)
0
3
6
24
35
25
Total S6
35
25
P-S6
70
55
p62
70
β-actin
F.
pS6/S6
Starvation (hr)
p62 /B-actin
Starvation (hr)

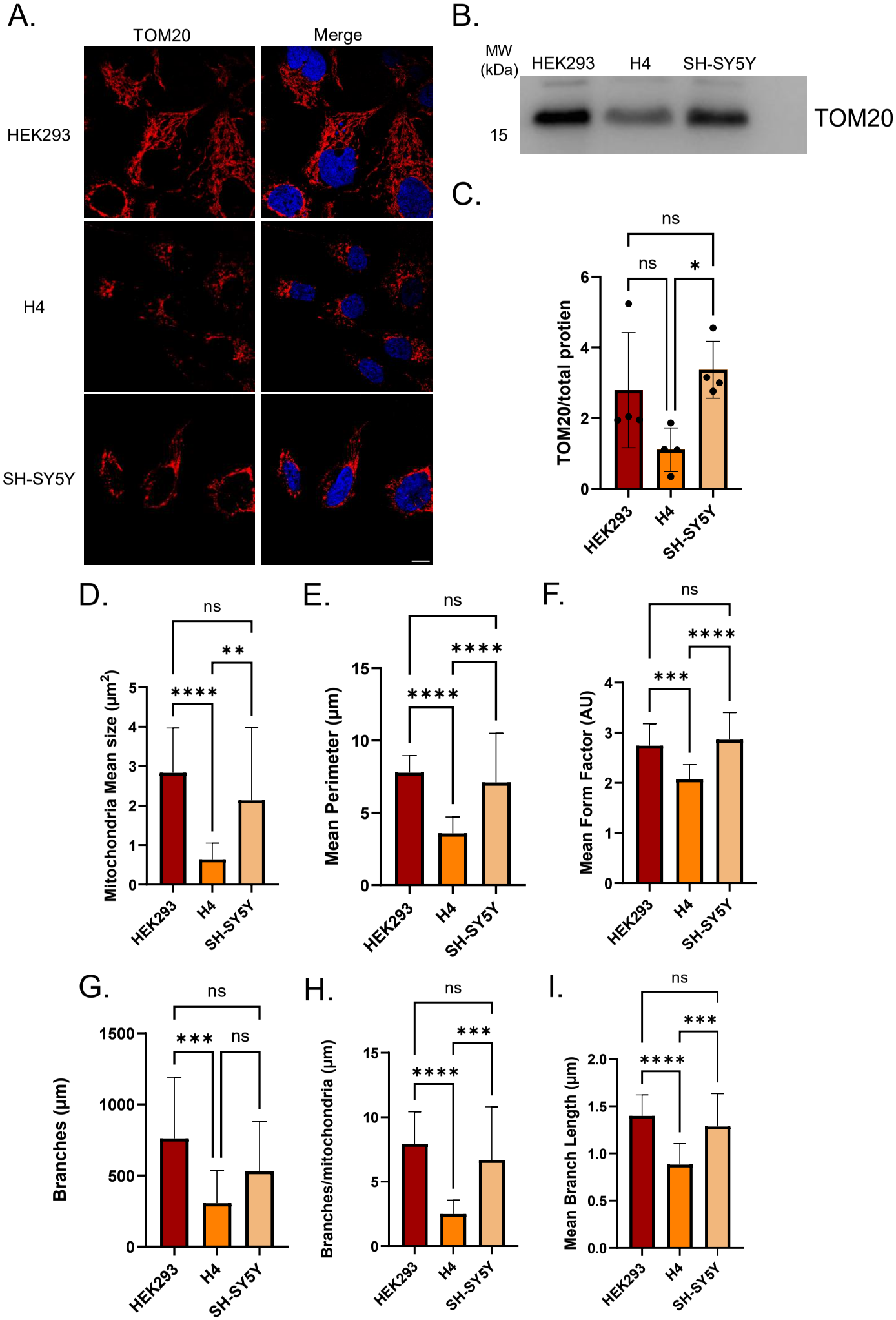
A.
TOM20
Merge
HEK293
H4
SH-SY5Y
B.
MW (kDa)
HEK293
H4
SH-SY5Y
15
TOM20
C.
TOM20/total protien
ns
ns
*
D.
Mitochondria Mean size (µm²)
ns
**
****
E.
Mean Perimeter (µm)
ns
****
****
F.
Mean Form Factor (AU)
ns
****
***
G.
Branches (µm)
ns
***
ns
H.
Branches/mitochondria (µm)
ns
***
****
I.
Mean Branch Length (µm)
ns
***
****
HEK293
H4
SH-SY5Y

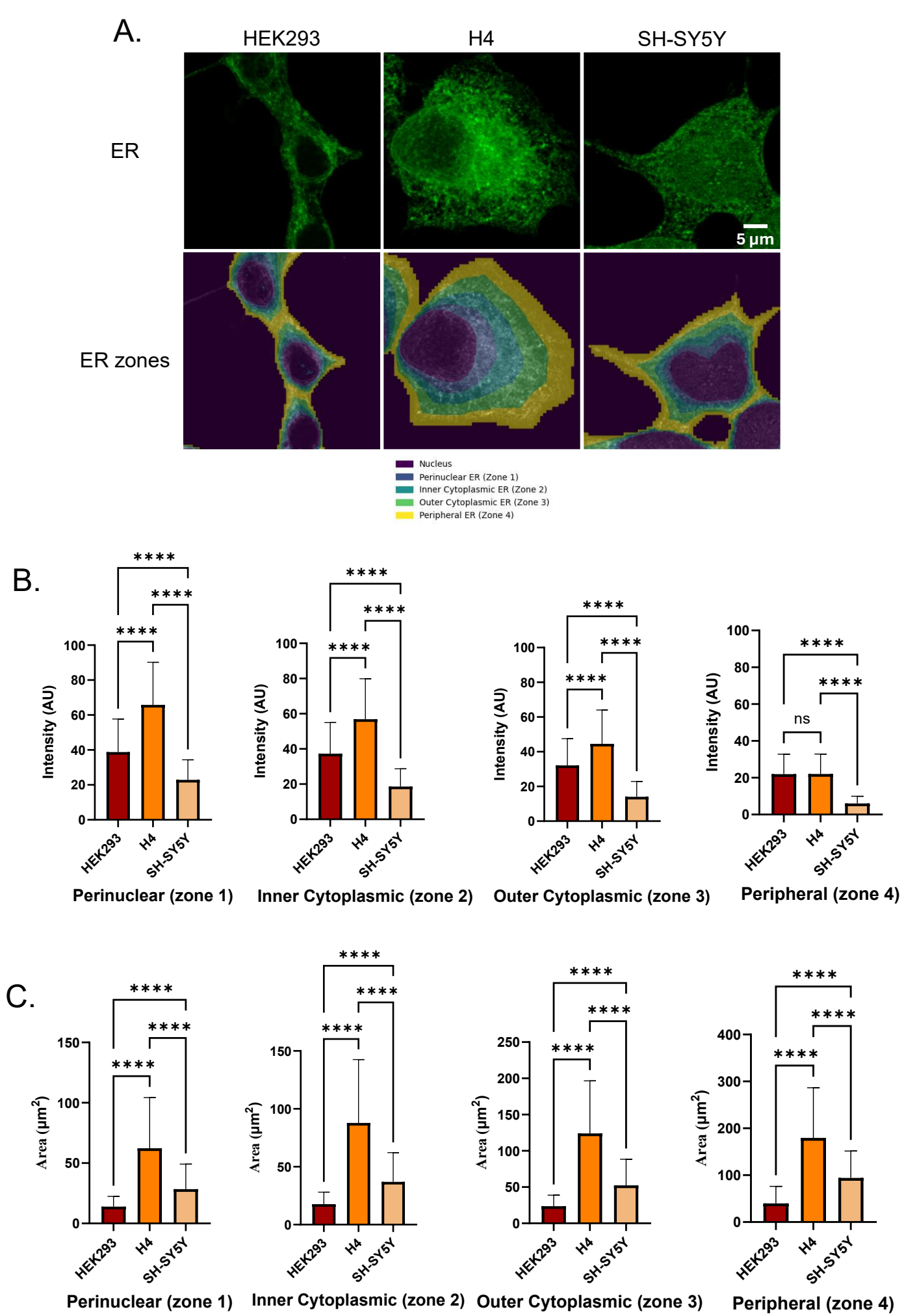
A.
HEK293
H4
SH-SY5Y
ER
5 µm
ER zones
Nucleus
Perinuclear ER (Zone 1)
Inner Cytoplasmic ER (Zone 2)
Outer Cytoplasmic ER (Zone 3)
Peripheral ER (Zone 4)
B.
Intensity (AU)
HEK293
H4
SH-SY5Y
****
ns
Perinuclear (zone 1)
Inner Cytoplasmic (zone 2)
Outer Cytoplasmic (zone 3)
Peripheral (zone 4)
C.
Area (µm²)
Perinuclear (zone 1)
Inner Cytoplasmic (zone 2)
Outer Cytoplasmic (zone 3)
Peripheral (zone 4)

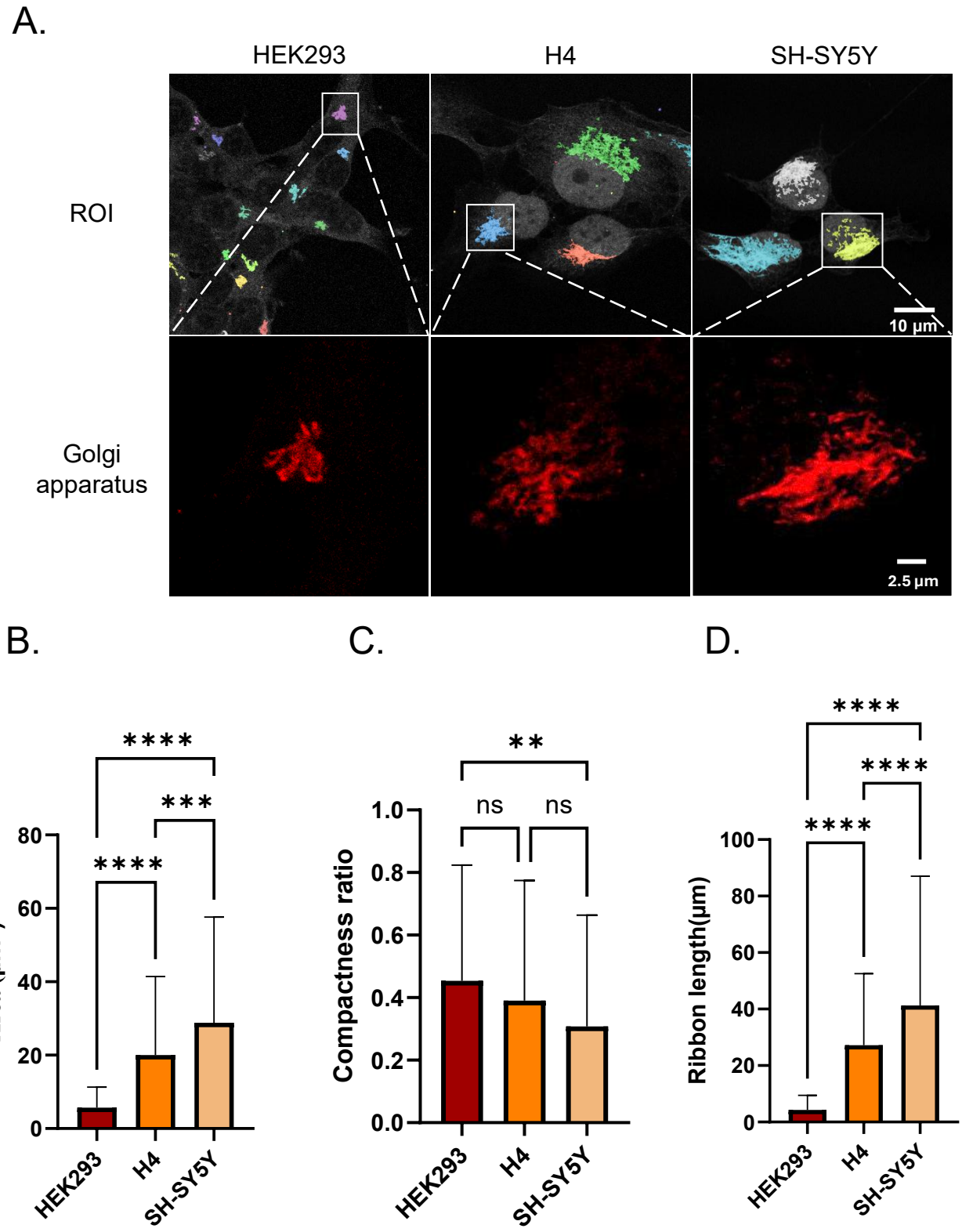
A.
HEK293
H4
SH-SY5Y
ROI
Golgi apparatus
10 μm
2.5 μm
B.
C.
D.
Area (μm²)
Compactness ratio
Ribbon length(μm)
****
***
**
ns
HEK293
H4
SH-SY5Y

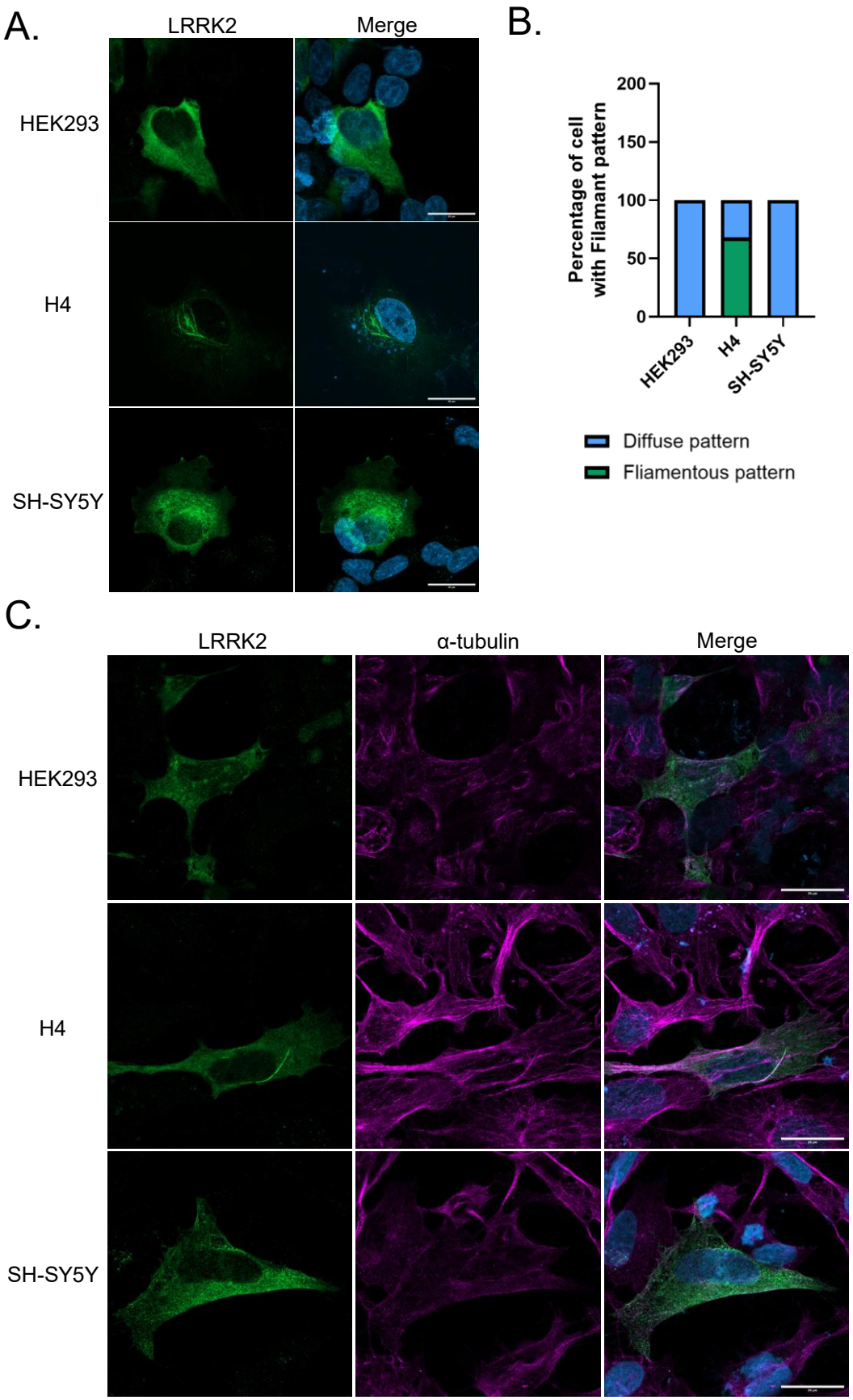
A.
LRRK2
Merge
HEK293
H4
SH-SY5Y
B.
Percentage of cell with Filamant pattern
200
150
100
50
0
HEK293
H4
SH-SY5Y
Diffuse pattern
Fliamentous pattern
C.
LRRK2
α-tubulin
Merge
HEK293
H4
SH-SY5Y

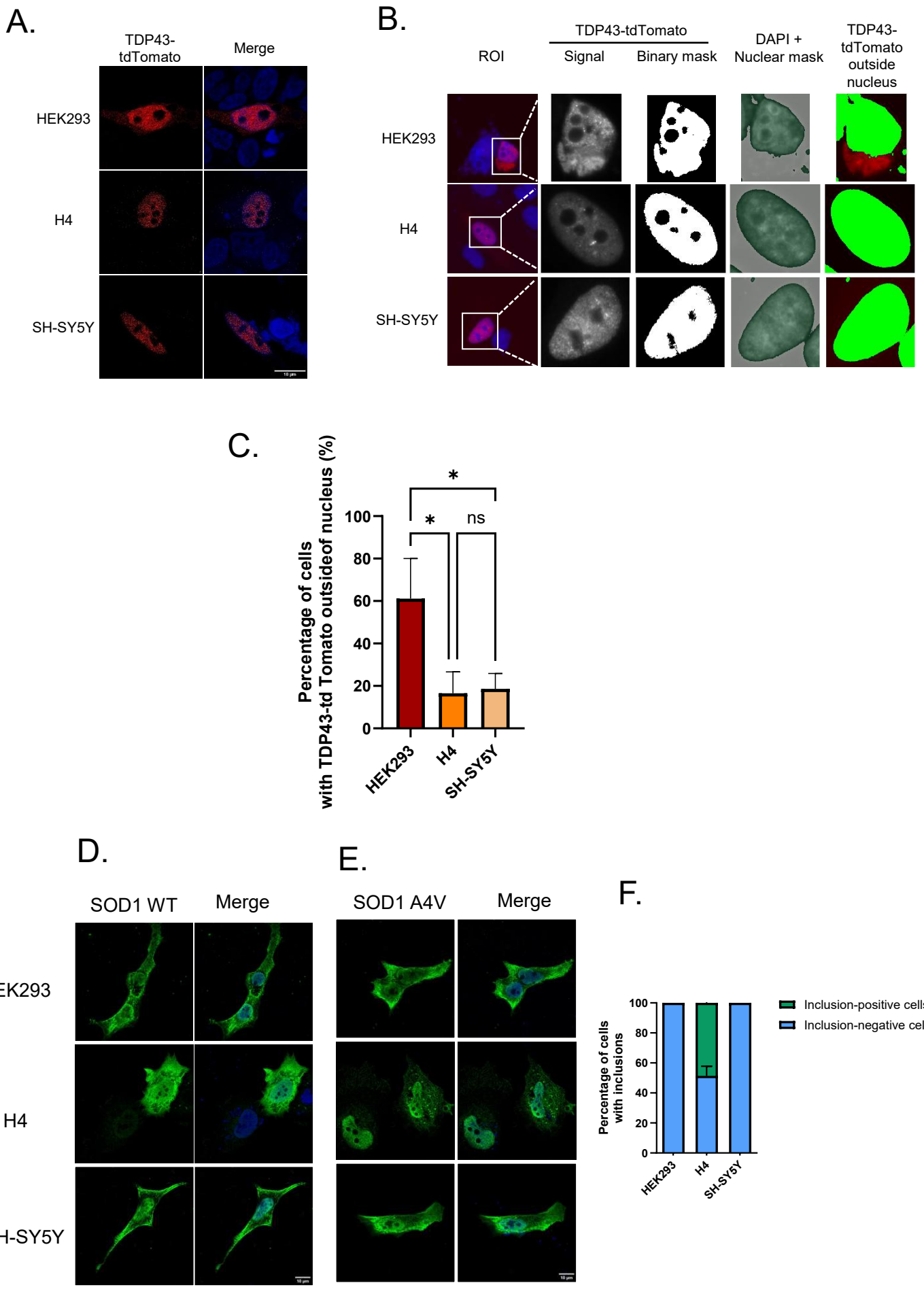
A.
TDP43-tdTomato
Merge
HEK293
H4
SH-SY5Y
B.
ROI
TDP43-tdTomato
Signal
Binary mask
DAPI + Nuclear mask
TDP43-tdTomato outside nucleus
HEK293
H4
SH-SY5Y
C.
Percentage of cells with TDP43-td Tomato outsideof nucleus (%)
100
80
60
40
20
0
*
*
ns
HEK293
H4
SH-SY5Y
D.
SOD1 WT
Merge
HEK293
H4
SH-SY5Y
E.
SOD1 A4V
Merge
F.
Percentage of cells with inclusions
100
80
60
40
20
0
HEK293
H4
SH-SY5Y
Inclusion-positive cells
Inclusion-negative cells

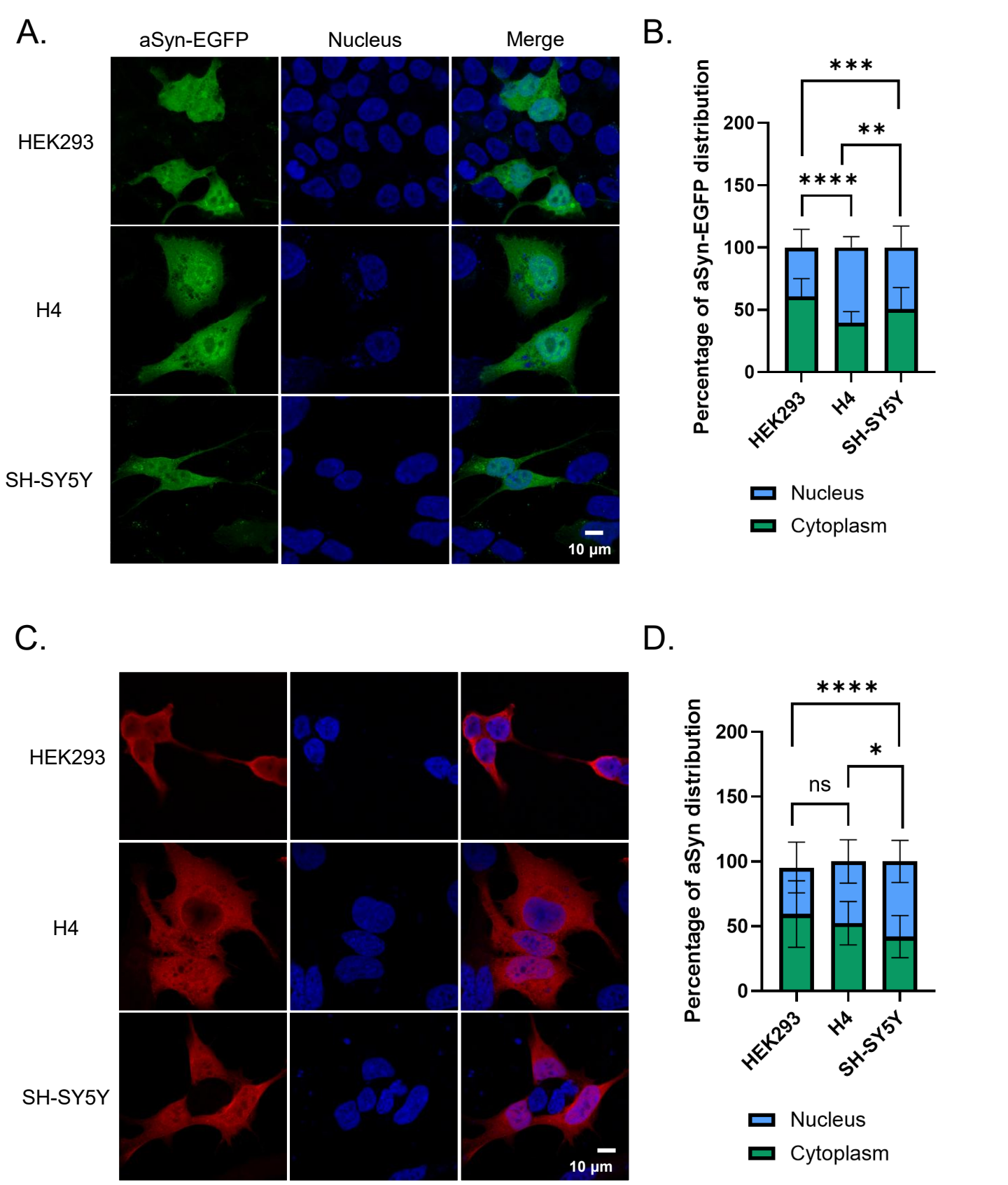
A.
aSyn-EGFP
Nucleus
Merge
HEK293
H4
SH-SY5Y
10 µm
B.
***
**
****
Percentage of aSyn-EGFP distribution
200
150
100
50
0
HEK293
H4
SH-SY5Y
Nucleus
Cytoplasm
C.
HEK293
H4
SH-SY5Y
10 µm
D.
****
*
ns
Percentage of aSyn distribution
200
150
100
50
0
HEK293
H4
SH-SY5Y
Nucleus
Cytoplasm

Table 1

Protein	Gene	Chromosome	Number of chromosomes per cell line
aSyn	*SNCA*	4q22.1	HEK293: 2 H4: 3 SH-SY5Y: 2
TDP-43	*TARDBP*	1q36.22	HEK293: 3 H4: 3 SH-SY5Y: 2
LRRK2	*LRRK2*	12q12	HEK293: 3 H4: 2 SH-SY5Y: 2
LAMP1	*LAMP1*	13q34	HEK293: 2 H4: 2 SH-SY5Y: 2
LC3	*MAP1LC3B*	16p24.2	HEK293: 2 H4: 3 SH-SY5Y: 2
SOD1	*SOD1*	21q22.11	HEK293: 5 H4: 3 SH-SY5Y: 2

Supplementary Files

This is a list of supplementary files associated with this preprint. Click to download.

- MoleculararchitecturedeterminesproteostasisresponsesNaturecommunicationSup.pdf